

## Article

# Statistical Characteristics of Geometry, Density and Porosity of Individual Ore Particles: A Case Study

Weiran Zuo <sup>1,2,\*</sup>, Yuqing Lu <sup>1</sup>, Jingwei Xu <sup>3</sup>, Weichao Liu <sup>1</sup> and Keqiang Chen <sup>4</sup>

<sup>1</sup> Zijin School of Geology and Mining, Fuzhou University, Fuzhou 350108, China

<sup>2</sup> Fujian Key Laboratory of Green Extraction and High-Value Utilization of New Energy Metals, Fuzhou University, Fuzhou 350108, China

<sup>3</sup> Jinan Heavy Machinery Joint-Stock Co., Ltd., Jinan 250109, China

<sup>4</sup> School of Resources and Civil Engineering, Northeastern University, Shenyang 110819, China

\* Correspondence: zuoweiran@fzu.edu.cn

**Abstract:** This study aims to develop a methodology to describe and predict the statistical characteristics of individual ore particles in terms of length, width, height, volume, mass, area, circularity, aspect ratio, density, and porosity. The mean value, standard deviation, and appropriate distribution function were calculated or identified for each data set of a given particle property in a given size fraction. It was found that the mean value and the standard deviation of the same particle property can either be predicted from particle size or be approximated by a constant. The best-fit distribution of each kind of particle property was identified by the Anderson–Darling test using Minitab software. Generally, the data sets with the same particle property but different size fractions and ore types follow the same distribution. A methodology was developed to predict the distribution of individual particle properties in a given size fraction by particle size, and the fitting quality is good in most cases. The statistical characteristics of individual ore particles can improve the precise processing of ore feed in concentrators, the preparation of feed samples for lab-scale testing, the calibration of image analysis of ore particle size distribution, etc.



**Citation:** Zuo, W.; Lu, Y.; Xu, J.; Liu, W.; Chen, K. Statistical Characteristics of Geometry, Density and Porosity of Individual Ore Particles: A Case Study. *Minerals* **2023**, *13*, 1298. <https://doi.org/10.3390/min13101298>

Academic Editors: Ugur Ulusoy and Onur Guven

Received: 11 July 2023

Revised: 29 September 2023

Accepted: 29 September 2023

Published: 7 October 2023



**Copyright:** © 2023 by the authors. Licensee MDPI, Basel, Switzerland. This article is an open access article distributed under the terms and conditions of the Creative Commons Attribution (CC BY) license (<https://creativecommons.org/licenses/by/4.0/>).

**Keywords:** statistical characteristics; geometry; density; porosity

## 1. Introduction

Unlike the uniform and stable material supply in manufacturing, heterogeneity is a common feature of rocks. As a result of geological genesis and processes, rocks from the same source vary from each other in terms of particle properties [1]. This heterogeneous feature of rock translates into variability when particulates of a given ore type are treated in mining operations, posing challenges from blasting to concentration [2]. Computer control of mineral processing plants requires continuous measurement of ore particle properties. Particle properties can be classified into two categories: material and morphological properties [3]. While the variability of material properties of ore particles, such as grade and structure, has become the focus of research for many years, the morphological properties have not yet gotten enough attention. However, the morphological properties of ore particles do have a significant influence on breakage [4], screening [5], and separation [6–8]. Measurement and analysis of the morphological properties' distribution in a sample are necessary to understand and interpret the effects of ore particles' heterogeneity. For example, the probability distribution of shape control attributes has to be assumed when the effect of particle shape on SAG mill charge motion is investigated in DEM simulation [9]. Although the value of particle shape has also been investigated experimentally under the background of mineral processing [3], there is a lack of methods to describe the probability distribution of shape parameters for natural ore particles.

In this study, a statistical study of the morphological properties of individual particles was conducted for two kinds of porphyry copper ores in terms of particle geometry, mass,

density, and porosity. The purpose of this study is to find appropriate distribution functions for each kind of property of ore particles and to develop a method to predict the distribution of individual ore particles' morphological properties. Therefore, the characteristics of the processing object of the mineral concentrator, i.e., geometry, density, and porosity of individual particles in ore feed, can be described and predicted well.

## 2. Materials and Methods

### 2.1. Ore Samples

This study investigated two kinds of porphyry copper ores from China: Ore A and Ore B. Ore A is a low-grade copper ore taken from a mine site in Fujian Province in southeast China. The ore sample has a notably high pyrite content and a small number of copper minerals, including digenite, covellite, chalcocite, and enargite. The majority of copper minerals are digenite. Quartz forms the primary gangue mineral with minor amounts of dickite and alunite.

Ore B was taken from a mine site in Heilongjiang Province in northeast China. The copper-bearing minerals include chalcopyrite, bornite, covellite, and cuprite. Chalcopyrite, as the most important form of copper sulfide minerals, is distributed in the gangue minerals as a microgranular star-shaped formation. Other minor metallic minerals include pyrite, magnetite, molybdenite, gold, etc. The nonmetallic minerals mainly consist of quartz, plagioclase, sericite, chlorite, calcite, apatite, and zircon.

Ore A sample was investigated with 9 size fractions, namely 53–63 mm, 45–53 mm, 37.5–45 mm, 31.5–37.5 mm, 26.5–31.5 mm, 22.4–26.5 mm, 19–22.4 mm, 16–19 mm, and 13.2–16 mm. In each size fraction, 180 particles were collected by random hand selection to measure different kinds of properties. The original intention for the Ore B sample was to conduct measurements with the same size fractions and particle numbers. Due to the lack of coarse particles, the Ore B sample of the top two size fractions was either excluded from the investigation (53–63 mm) or reduced to 30 particles (45–53 mm). This study was conducted with 1620 Ore A particles and 1290 Ore B particles.

### 2.2. Measurement of Geometry, Density, and Porosity for Individual Particle

In this study, 7 kinds of geometry properties were measured for the individual ore particles, as well as density/specific gravity ( $X_{sg}$ ) and porosity ( $X_p$ ). The mass of each ore particle ( $X_m$ ) was also measured as a byproduct. The geometry properties of individual ore particles considered here are length ( $X_l$ ), width ( $X_w$ ), height ( $X_h$ ), area ( $X_s$ ), volume ( $X_v$ ), circularity ( $X_c$ ), and aspect ratio ( $X_{ar}$ ).

Except for porosity, all the particle properties mentioned above were measured for each ore particle (1620 particles for Ore A and 1290 particles for Ore B). The porosity analysis was only conducted for the 180 Ore A particles at 22.4–26.5 mm.

The geometry properties, mass, and specific gravity of individual ore particles were measured by a combination of vernier calipers, image analysis, and density balance. Firstly, each particle was placed on a plane in the posture with the lowest gravity center. The thickness of each particle in the vertical direction of this most stable posture was deemed the particle's height and measured directly using a digital vernier caliper. After that, the particle was placed on a shadowless panel lamp, still in this posture, to take pictures of their projections. Some geometry parameters of ore particles were measured from these projections, including length, width, area, circularity, and aspect ratio, using the well-known scientific image processing software ImageJ (version 1.54f, National Institutes of Health, Bethesda, MD, USA).

The ImageJ software can export length and width values for the projected shape in three modes: bounding rectangle, fit ellipse, and Feret's diameter/Minferet. This study found that the width values in all three modes are larger than the average particle size determined by mechanical sieving. Among the three modes, the fit ellipse mode could export width values closest to the mechanical sieved particle size. Therefore, the major and minor axes of the best-fitted ellipse are defined as the length and width of the ore particle.

The concept of particle length and width defined by the fit ellipse is illustrated in Figure 1. Examples of particle projection pictures taken with a shadowless panel lamp are given in Figure 2 for Ore A and Ore B.

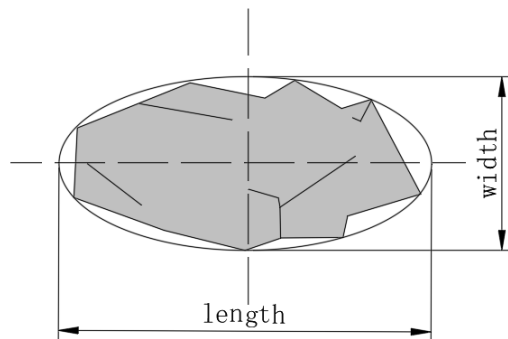


**Figure 1.** Particle length and width defined by fit ellipse.

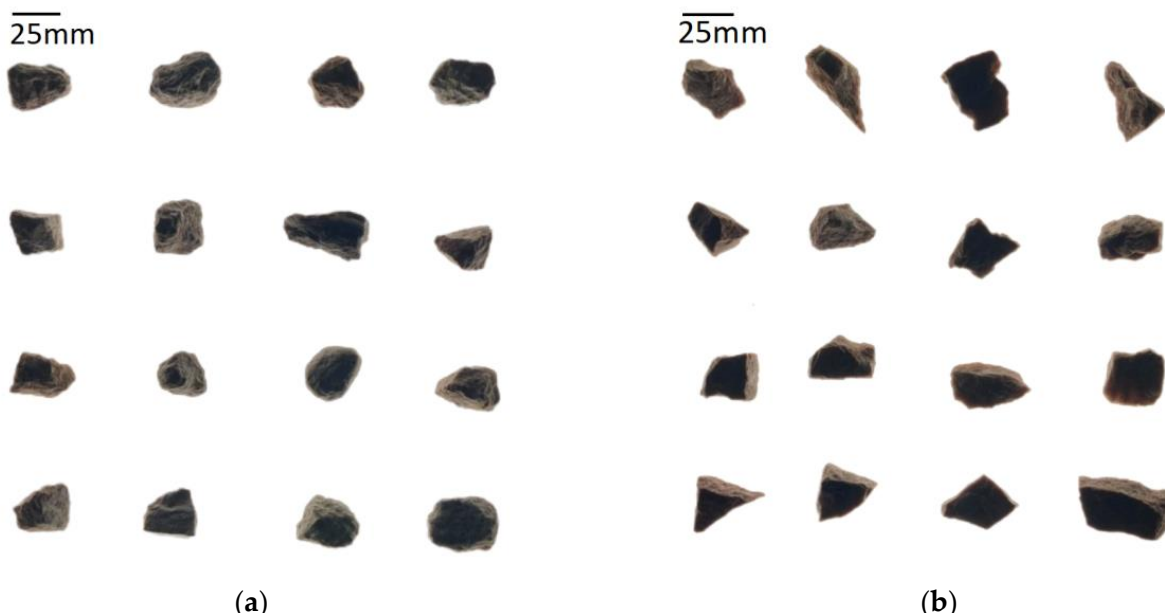


**Figure 2.** Projections of Ore A (a) and Ore B (b) particles in 22.4–26.5 mm.

The definitions of circularity and aspect ratio used in ImageJ are provided below:

Circularity ( $4\pi \times \frac{\text{Area}}{\text{Perimeter}^2}$ ), is a value between 0 and 1. As the value approaches 0, it indicates an increasingly elongated shape, while a value of 1 indicates a perfect circle.

Aspect ratio is the ratio of the major and minor axes of a particle's fitted ellipse. The minimum aspect ratio is 1, and increasing this value indicates that the shape is increasingly elongated.

Finally, the mass of each ore particle in air and water was measured by a density balance. The volume of every single particle was calculated by comparing its mass in air and in water. Then, the specific gravity (SG) was calculated by dividing the ore particle mass by its volume. The porosity of particles was analyzed with MesoMR23-060H, a low-field nuclear magnetic resonance (NMR) analyzer for rock produced by Suzhou Niumag Analytical Instrument Corporation in China.

### 2.3. Descriptive Statistics of Individual Particles' Properties

It is important to understand a data set's central tendency, variability, and distribution when performing descriptive statistics. The central tendency concerns the averages of the values. The mean, median, and mode are 3 ways of finding the average. The variability

concerns how spread out the values are. The range, standard deviation, and variance reflect different aspects of the spread. The distribution concerns the frequency of each value.

In this study, the values of each ore particle property for each size fraction of a given ore type form a separate property-size data set. The descriptive statistics of each data set are investigated in the way summarized below:

- Central tendency is represented by the mean of each data set.
- Variability is represented by the standard deviation and coefficient of variation of each data set.
- Appropriate distribution for each data set is identified from 14 candidate distributions by Minitab software.

Here, the coefficient of variation (COV) represents the ratio of the standard deviation (SD) to the mean of the data. The candidate distributions are normal, lognormal, 3-parameter lognormal, exponential, 2-parameter exponential, Weibull, 3-parameter Weibull, smallest extreme value, largest extreme value, gamma, 3-parameter gamma, logistic, log-logistic, and 3-parameter log-logistic. The probability density functions (PDF) of the 14 candidate distributions, as well as the distribution identification method introduced in Section 2.4, can be found in the support document of Minitab [10].

#### 2.4. Individual Distribution Identification

To identify the distribution of a given data set, Minitab software calculates Anderson–Darling statistics ( $A^2$ ) to perform the goodness-of-fit test (GFT). Based on the Anderson–Darling statistic ( $A^2$ ) obtained, Minitab calculates the  $p$ -value for the candidate distribution function. Usually, a significance level (denoted as  $\alpha$ ) of 0.05 works well. A significance level of 0.05 indicates a 5% risk of concluding that the data do not follow the distribution when they do follow the distribution. Therefore, if the  $p$ -value is greater than the significance level (0.05), it fails to reject the null hypothesis ( $H_0$ ) and can then be assumed that the data follows the distribution.

### 3. Results and Discussion

#### 3.1. Relationship of the Mean of Individual Ore Particles' Properties to Particle Size

The mean values of length ( $X_l$ ), width ( $X_w$ ), height ( $X_h$ ), area ( $X_s$ ), volume ( $X_v$ ), circularity ( $X_c$ ), aspect ratio ( $X_{ar}$ ), mass ( $X_m$ ), specific gravity ( $X_{sg}$ ), and porosity ( $X_p$ ) of individual ore particles are represented by  $\mu_l$ ,  $\mu_w$ ,  $\mu_h$ ,  $\mu_s$ ,  $\mu_v$ ,  $\mu_r$ ,  $\mu_{ar}$ ,  $\mu_m$ ,  $\mu_{sg}$ , and  $\mu_p$ , respectively.

##### 3.1.1. Ore Particle Properties of Length, Width, and Height

Figure 3 provides the relationships of the  $\mu_l$ ,  $\mu_w$ , and  $\mu_h$  values to  $\mu_x$ . Here, the symbol  $\mu_x$  is designated as the geometric mean size of each size fraction of ore particles. The trendline equations and corresponding  $R$ -square values of the equations of the relationships in Figure 3 are listed in Table 1.  $R$ -square, or determination coefficient, is a value between 0 and 1, which quantifies the reliability of the trendline equations. The trendline is more reliable when its  $R$ -square is at or close to 1. As given in Table 1, the  $R$ -square values of all the trendlines in Figure 3 are close to 1, indicating the fittings of trendline equations are well.

As expected, the  $\mu_w$  values of both the two ore types have a significant linear relationship with the  $\mu_x$  value since whether an individual particle could pass the sieve aperture is strongly dependent on the width of the particle. The slope of the  $\mu_w - \mu_x$  trendlines indicates that the width of Ore A and Ore B particles (the central axis of the fitted ellipse of the particle's projection) is 1.12 times and 1.19 times their sieve-determined size on average, respectively. Furthermore, the  $\mu_l$  and  $\mu_h$  values of Ore A also show significant linear relations to the  $\mu_x$  value (see Figure 3a). The slopes of the linear trendlines suggest that the average length, width, and height of Ore A particles have a constant ratio of 1.56:1.12:0.74 (approximate 1.4:1:2/3) in the span between 13.2 mm and 63 mm. However, such self-similarity in dimensions was not found for the Ore B sample. Unlike the  $\mu_w$  value, the  $\mu_l$  and  $\mu_h$  values of Ore B present a nonlinear relation to  $\mu_x$ , as shown in Figure 3b. Compared with Ore A, the ratio of  $\mu_l$  to  $\mu_w$  for Ore B is slightly smaller at the finer end

and bigger at the coarser end. Meanwhile, the  $\mu_h$  value of Ore B particles is reduced significantly relative to the  $\mu_w$  value, especially for coarser particles. The possible reason for this phenomenon is discussed later in Section 3.1.2.

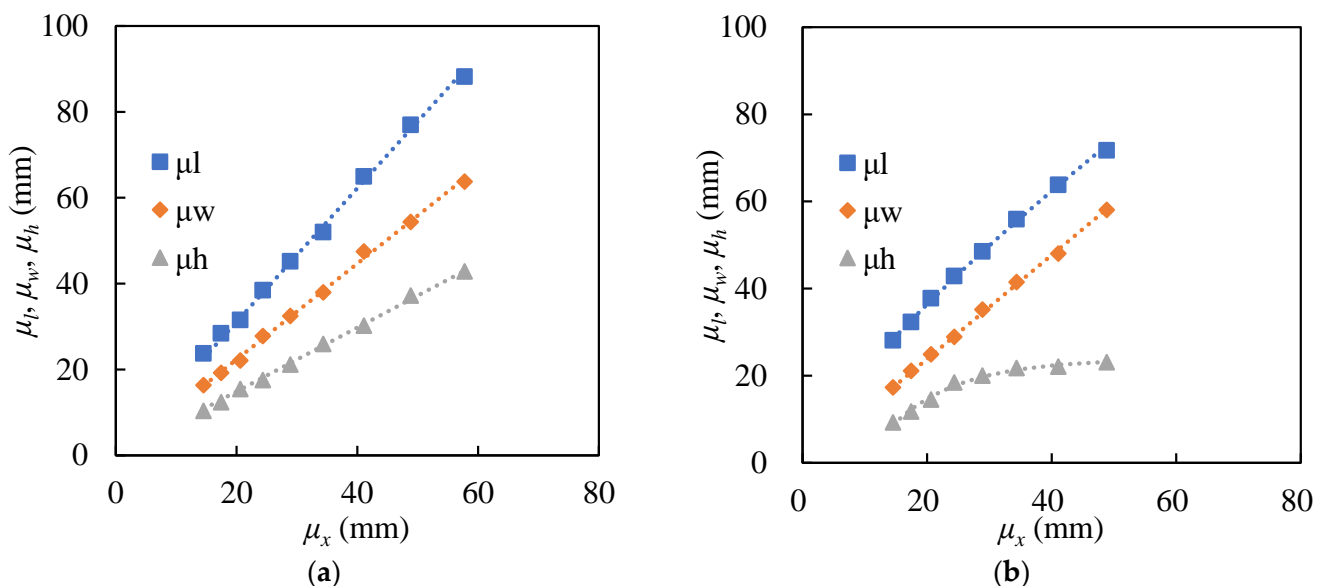


**Figure 3.** Relationships of  $\mu_l$ ,  $\mu_w$ , and  $\mu_h$  values to  $\mu_x$  values of different sizes for Ore A (a) and Ore B (b).

**Table 1.** Empirical models for the relation between a particle's property mean value to the  $\mu_x$ .

Item	Ore A		Ore B	
	Model	R <sup>2</sup>	Model	R <sup>2</sup>
$\mu_l$	$1.56\mu_x$	0.997	$3.54\mu_x^{0.78}$	0.999
$\mu_w$	$1.12\mu_x$	0.998	$1.19\mu_x$	0.999
$\mu_h$	$0.74\mu_x$	0.998	$23.81 \times (1 - \exp(-0.09(\mu_x - 9.51)))$	0.990
$\mu_v$	$6.25\mu_x^{2.98} \times 10^{-4}$	1.000	$2.49\mu_x^{2.56} \times 10^{-3}$	0.996
$\mu_m$	$1.65\mu_x^{2.98} \times 10^{-3}$	1.000	$5.91\mu_x^{2.59} \times 10^{-3}$	0.995
$\mu_s$	$1.50\mu_x^{1.97} \times 10^{-2}$	0.998	$3.46\mu_x^{1.77} \times 10^{-2}$	0.999
$\mu_{sg}$	$2.644 \pm 0.010^*$	/	$2.73 \times (1 - \exp(-0.21\mu_x))$	0.927
$\mu_c$	$0.730 \pm 0.006^*$	/	$0.58\mu_x^{0.064}$	0.930
$\mu_{ar}$	$0.57 \times \exp(-0.12\mu_x) + 1.38$	0.698	$2.91\mu_x^{-0.22}$	0.974

\* represents the 95% confidence interval.

### 3.1.2. Ore Particle Properties of Volume, Mass, and Area

The relationships of  $\mu_v$ ,  $\mu_m$ , and  $\mu_s$  values to  $\mu_x$  for Ore A and Ore B are given in Figure 4. The trendline equations and corresponding R-square values of the equations of the relationships in Figure 4 are listed in Table 1. It can be found that the  $\mu_v$ ,  $\mu_s$  values of Ore A particles are positively proportional to the cube or square of  $\mu_x$ , respectively. This fact confirms again that Ore A particles are self-similar in dimensions across a wide size range. Due to the stability of the specific gravity of Ore A particles, as given in Section 3.1.3, the  $\mu_m$  value of Ore A also has a cubic relationship with its  $\mu_x$  value.

Meanwhile, the  $\mu_v$ ,  $\mu_m$ , and  $\mu_s$  values of Ore B particles present power relationships to the  $\mu_x$  value as well. However, the powers of the  $\mu_v - \mu_x$ ,  $\mu_m - \mu_x$ , and  $\mu_s - \mu_x$  relationships of Ore B are approximately 2.6, 2.6, and 1.8, respectively, being less than the powers of 3, 3, and 2 for the Ore A sample (as given in Table 1). This result is consistent with the nonlinearity of the  $\mu_l - \mu_x$  and  $\mu_h - \mu_x$  relationships of Ore B discussed above.

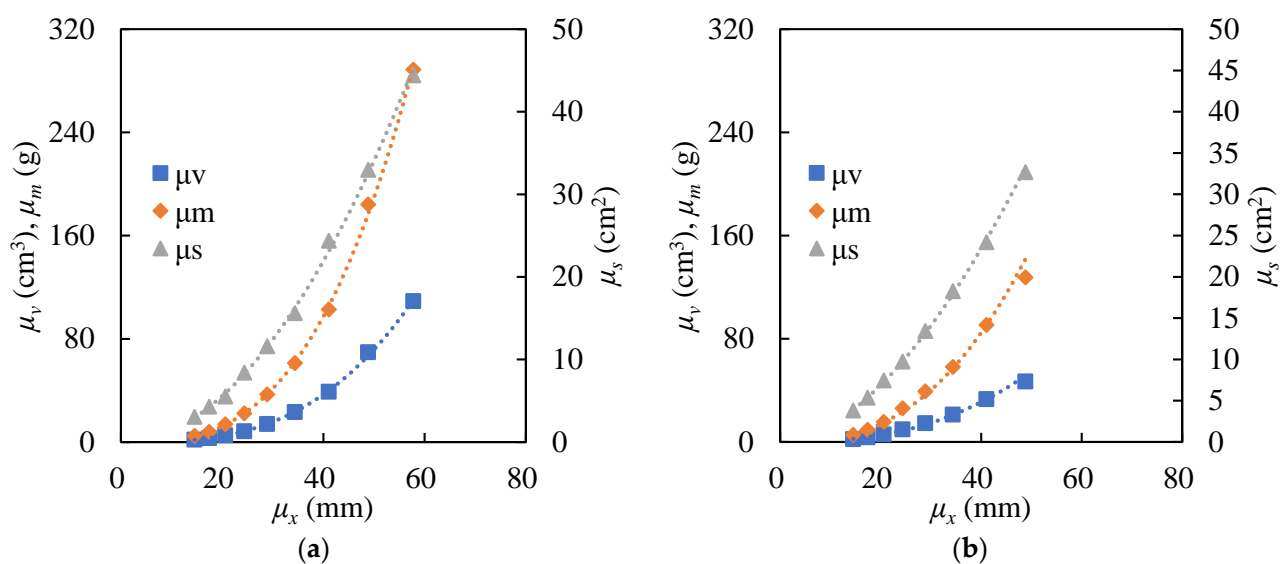


**Figure 4.** Relation of  $\mu_v$ ,  $\mu_m$ ,  $\mu_s$  values to  $\mu_x$  values of different sizes for Ore A (a) and Ore B (b).

To explore the reason why the relation of  $\mu_l$ ,  $\mu_h$ ,  $\mu_v$ ,  $\mu_m$ , and  $\mu_s$  values to  $\mu_x$  value of the two ore types distinguished from each other, the preparation histories of the two kinds of samples were examined carefully. The primary discrepancy between the two ores was found in the crushing method. The Ore A sample was collected and selected directly from the secondary cone crusher product at the mine site. Ore B sample was also collected from the product of a secondary cone crusher at the mine site, but extra breakage using a lab jaw crusher had been conducted before the measurement of ore properties. Considering that the discharge gap of the lab jaw crusher is much smaller than that of the industrial secondary crusher, the maximum height of progeny particles in the Ore B sample broken by the lab jaw crusher would be seriously limited. As shown in Figure 3b, when the  $\mu_x$  value increases from 28.9 mm to 48.8 mm, the  $\mu_h$  value only increases from 20.0 mm to 23.1 mm. The difference in the  $\mu_l - \mu_x$  relation between Ore A and Ore B might also be attributed to the difference in the crushing method. As a result, the relations of  $\mu_v$ ,  $\mu_m$ , and  $\mu_s$  values to the  $\mu_x$  value of Ore B diverge from Ore A. To confirm this hypothesis, a group of as-received Ore A particles were broken with a lab jaw crusher and sieved, referred to as Ore A' below. The  $\mu_m - \mu_x$  relationships of Ore A' as well as another three ore types are exhibited in Figure 5 for comparison. The  $\mu_m - \mu_x$  data of another three ore samples were by-products of a previous published work [11]. The three ore types, here designated as Ore 1, Ore 2, and Ore 3, represent a gold-copper ore, a copper-silver-gold ore, and a hematite ore, respectively. Among these three ore types, the Ore 1 sample and Ore 2 sample were prepared from industrial crusher products directly, while the Ore 3 sample experienced lab jaw crushing. As indicated by the trendlines in Figure 5, the  $\mu_m - \mu_x$  data of Ore 1 and Ore 2 samples approximately follow a cubic power relation, while the power parameters of Ore 3 and Ore A' are only approximately 2.7. The reason for this phenomenon can be attributed to the fact that, within the size range concerned in this paper, lab jaw crushers can provide more points of loading in compressive failure for larger feed particles, imposing limits on the dimensions of progeny particles [6]. However, more research should be carried out to further explore the influence of the crushing method, ore texture, and other factors on the dimensions of ore particles.

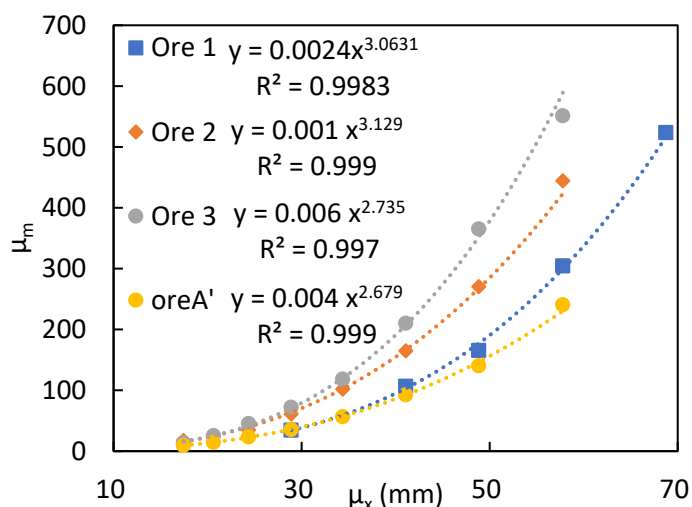


**Figure 5.**  $\mu_m - \mu_x$  relations of Ore 1, Ore 2, Ore 3, and Ore A'.

### 3.1.3. Ore Particle Properties of Specific Gravity, Circularity, and Aspect Ratio

Figure 6 provides the relations of the  $\mu_{sg}$ ,  $\mu_c$ , and  $\mu_{ar}$  values to the  $\mu_x$  value for Ore A and Ore B. The trendline equations and corresponding  $R^2$ -square values of the equations of the relationships in Figure 6 are listed in Table 1. Linear regression analyses by Excel were applied to judge the relations of  $\mu_{sg}$  and  $\mu_c$  to  $\mu_x$  for Ore A. Analysis of variance confirms that the slopes of both  $\mu_{sg} - \mu_x$  relationship and  $\mu_c - \mu_x$  relationship are 0 ( $p$ -value  $>> 0.05$ ). In other words, the  $\mu_{sg}$  value and  $\mu_c$  value of the Ore A sample keep constant statistically in the size range from 13.2 to 63 mm. The 95% confidence intervals of  $\overline{\mu}_{sg}$  and  $\overline{\mu}_c$  are  $2.643 \pm 0.010$  and  $0.730 \pm 0.006$ , respectively. Overall, the variation of the  $\mu_{ar}$  value of the Ore A sample is not significant, and it remains at nearly 1.39 when  $\mu_x$  is no less than 24.4 mm. However, when the  $\mu_x$  value reduces to below 24.4 mm, the  $\mu_{ar}$  value of the Ore A sample increases slightly up to 1.49. This phenomenon implies that the “self-similarity” of the Ore A sample in dimensions may not be retained as the particle size reduces to a finer extent. The  $\mu_{ar} - \mu_x$  relation for the Ore A sample can be fitted with the exponential empirical model as given in Table 1, with the  $R^2$ -square value being 0.787.

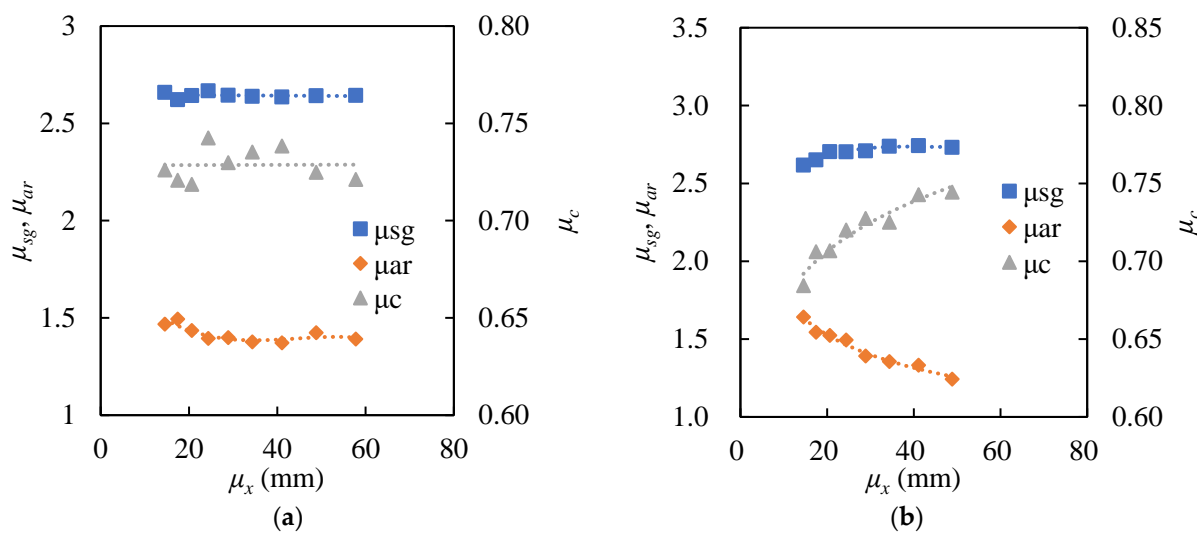


**Figure 6.** Relation of  $\mu_{sg}$ ,  $\mu_c$ ,  $\mu_{ar}$ , values to  $\mu_x$  values of different sizes for Ore A (a) and Ore B (b).

On the other hand, Figure 6b indicates that the  $\mu_{ar}$  value of the Ore B sample decreases significantly from 1.54 to 0.24 when  $\mu_x$  increases from 14.5 mm to 48.8 mm. This is consistent with the changing trend of  $\mu_l$  and  $\mu_w$  in the Ore B sample. The result indicates that particles

in both Ore A and Ore B samples have a tendency to be elongated as particle size becomes finer. It can be found that the  $\mu_c$  value of the Ore B sample increases with the increase in  $\mu_x$  value because less elongated particles have higher circularity. As shown in Figure 6b, both the  $\mu_c - \mu_x$  and  $\mu_{ar} - \mu_x$  relationships of the Ore B sample could be predicted by the power model. Unlike Ore A, it can be found that the  $\mu_{sg}$  value of Ore B also presents slight variation as the particle size decreases. As the  $\mu_x$  value decreases from 48.8 mm to 14.5 mm, the  $\mu_{sg}$  value is reduced from 2.73 to 2.62. A possible reason for this trend is that the softer but less dense component of Ore B was broken selectively during crushing, resulting in the concentration of a light component in finer-size fractions. On the contrary, such selective breakage has not been observed for the Ore A sample. The  $\mu_{sg}$  value of Ore B can be predicted from the  $\mu_x$  value with an exponential empirical model, as given in Table 1.

### 3.2. Relationship of the Variability of Individual Ore Particles' Properties to Particle Size

This study investigates the variability of individual ore particles' properties using SD and COV. The advantage of COV over SD is that COV is a useful statistic for comparing the degree of variability from one data series to another, even if the means are drastically different from one another. SD is discussed in this study because it is incorporated in the prediction of distribution function parameters in Section 3.4.

The SD and COV of length ( $X_l$ ), width ( $X_w$ ), height ( $X_h$ ), area ( $X_s$ ), volume ( $X_v$ ), circularity ( $X_c$ ), aspect ratio ( $X_{ar}$ ), mass ( $X_m$ ), and specific gravity ( $X_{sg}$ ) of individual ore particles are represented by the symbols of  $SD_l$ ,  $SD_w$ ,  $SD_h$ ,  $SD_s$ ,  $SD_v$ ,  $SD_c$ ,  $SD_{ar}$ ,  $SD_m$ , and  $SD_{sg}$ , and the symbols of  $COV_l$ ,  $COV_w$ ,  $COV_h$ ,  $COV_s$ ,  $COV_v$ ,  $COV_c$ ,  $COV_{ar}$ ,  $COV_m$ , and  $COV_{sg}$ , respectively.

#### 3.2.1. Ore Particle Properties of Length, Width, and Height

Figures 7 and 8 provide the relations of the  $SD_l$ ,  $SD_w$ ,  $SD_h$ ,  $COV_l$ ,  $COV_w$ , and  $COV_h$  values to  $\mu_x$  for Ore A and Ore B. Some data points in these two figures were identified as outliers and represented by hollow symbols in the figures. Most of the outliers are in the 45–53 mm size fraction of Ore B since the number of particles measured in this size fraction was as low as 30. A similar situation also occurs in the SD and COV values of other particle properties, as illustrated in Sections 3.2.2 and 3.2.3. Empirical models of the  $SD - \mu_x$  relations for all kinds of particle properties except porosity are summarized in Table 2.

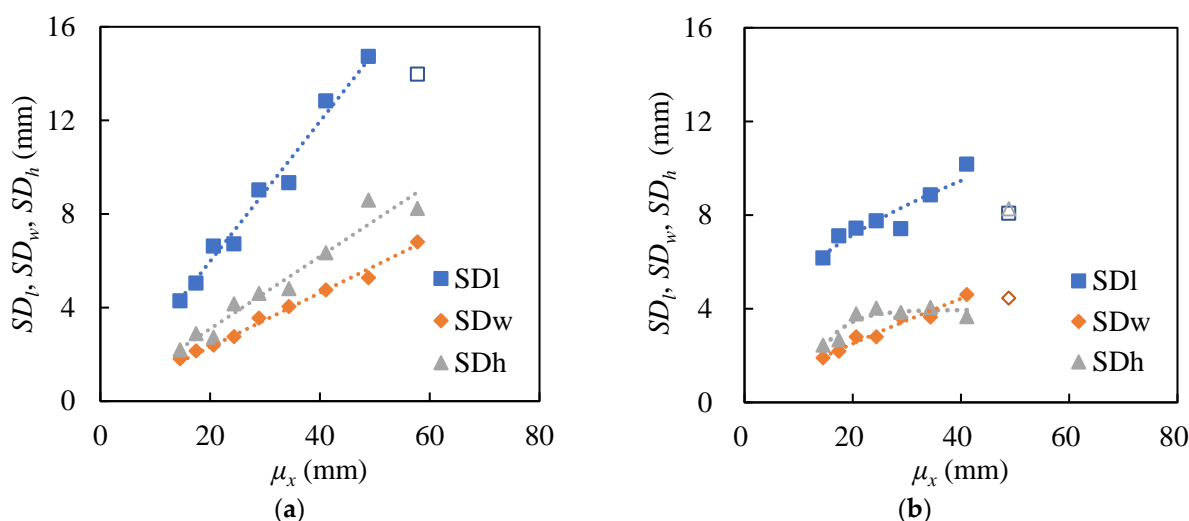


**Figure 7.** Relationship of  $SD_l$ ,  $SD_w$ , and  $SD_h$  values to  $\mu_x$  values of different sizes for Ore A (a) and Ore B (b). (Hollow symbol represents the outlier of the data series with the same shape).

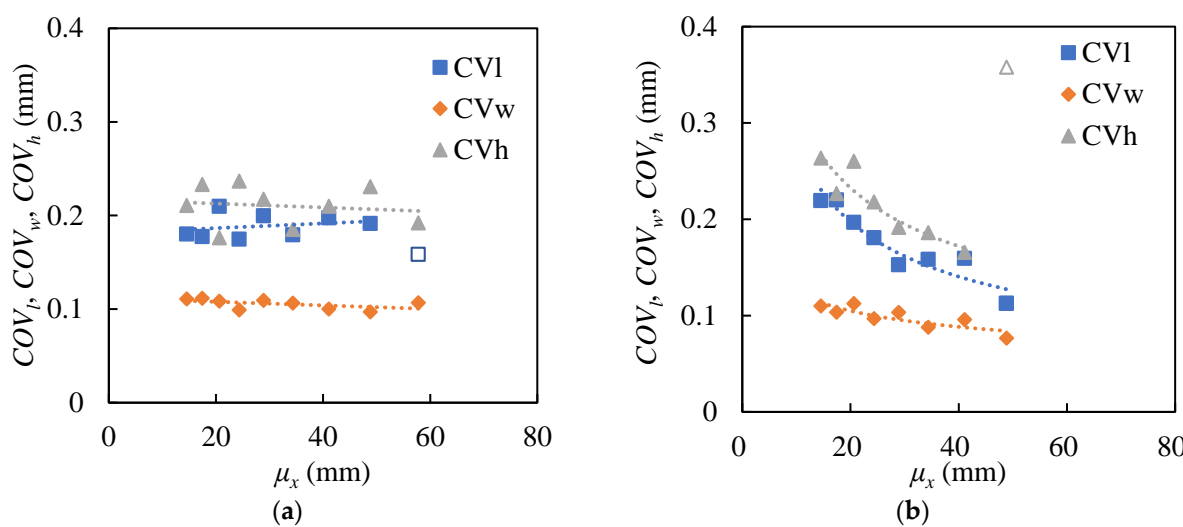


**Figure 8.** Relationship of  $COV_l$ ,  $COV_w$ , and  $COV_h$  values to  $\mu_x$  values of different sizes for Ore A (a) and Ore B (b). (Hollow symbol represents the outlier of the data series with the same shape).

**Table 2.** Empirical models for the relation between particle property's SD to  $\mu_x$ .

SD	Ore A		Ore B	
	Model	R <sup>2</sup>	Model	R <sup>2</sup>
$SD_l$	$0.30\mu_x$	0.980	$2.13\mu_x^{0.40}$	0.871
$SD_w$	$0.12\mu_x$	0.989	$0.22\mu_x^{0.82}$	0.964
$SD_h$	$0.15\mu_x$	0.948	$3.95 \times (1 - \exp(-0.22(\mu_x - 10.60)))$	0.884
$SD_v$	$1.75\mu_x^{2.96} \times 10^{-4}$	0.999	$1.36\mu_x^{2.35} \times 10^{-3}$	0.991
$SD_m$	$4.32\mu_x^{2.99} \times 10^{-4}$	0.999	$3.07\mu_x^{2.40} \times 10^{-3}$	0.990
$SD_s$	$3.24\mu_x^{2.00} \times 10^{-3}$	0.993	$1.73\mu_x^{1.52} \times 10^{-2}$	0.981
$SD_{sg}$	$0.097 \pm 0.013^*$	-	$13.65 \times \exp(-0.28\mu_x) + 0.041$	0.983
$SD_c$	$0.081\mu_x^{-0.12}$	0.346	$0.15\mu_x^{-0.31}$	0.879
$SD_{ar}$	$0.51\mu_x^{-0.18}$	0.649	$2.41\mu_x^{-0.67}$	0.968

\* represents the 95% confidence interval.

It can be seen from Figure 7a that the values of  $SD_l$ ,  $SD_w$ , and  $SD_h$  of the Ore A sample have a positive linear relation to  $\mu_x$ . In addition, Figure 8a indicates that the values of  $COV_l$ ,  $COV_w$ , and  $COV_h$  keep roughly the same at different size fractions, being approximately 0.192, 0.104, and 0.208, respectively. The constant COV values agree with the self-similarity in dimensions of the Ore A sample discussed in Section 3.1. On the other hand, the  $SD_l$  and  $SD_w$  values of Ore B can be predicted with the power model, while the  $SD_h - \mu_x$  relation is fitted well by the exponential relationship, as shown in Figure 7b and given in Table 2. Unlike Ore A, the COV values of Ore B are not constant and decrease with the increase in  $\mu_x$  (Figure 8b). What Ore A and Ore B have in common is that the values of COV have the order of  $COV_h > COV_l > COV_w$ . The smallest variation in particle width can be attributed to the fact that the width of individual particles in each size fraction is restricted strictly by the size of the sieve apertures. Possibly because of the limit of discharge gap of the lab jaw crusher, the variability of particle properties (length, width, and height) of Ore B is slighter than that of Ore A at the coarser end.

### 3.2.2. Ore Particle Properties of Volume, Mass, and Area

The relations of the  $SD_v$ ,  $SD_m$ ,  $SD_s$ ,  $COV_v$ ,  $COV_m$ , and  $COV_s$  values to  $\mu_x$  for Ore A and Ore B are given in Figures 9 and 10. It can be found that all the SD values in these two figures have a powerful relationship with the  $\mu_x$  value, as listed in Table 2. As for Ore A, the power parameters of the models for the relation of  $SD_v$ ,  $SD_m$ , and  $SD_s$  to  $\mu_x$  are very close to 3, 3, and 2, respectively, as shown in Table 2. Therefore, the  $COV_v$ ,  $COV_m$ , and

$COV_s$  values of Ore A keep roughly constant at different size fractions as well, being 0.27, 0.27, and 0.23 on average, respectively. As for Ore B, the power parameters of the  $SD - \mu_x$  models are obviously less than 3 or 2, being approximately 2.4, 2.4, and 1.5, respectively (Table 2). Accordingly, the  $SD_v$ ,  $SD_m$ , and  $SD_s$  values of Ore B particles are much less than those of Ore A at the same size fraction, and the  $COV_v$ ,  $COV_m$ , and  $COV_s$  values of Ore B decrease with the increase in  $\mu_x$ . This trend conforms to the observation introduced in Section 3.1 that Ore B particles do not have self-similarity in dimension. Figure 10 also indicates that the relative variability of  $COV_v$  and  $COV_m$  for both ore samples is close to each other and higher than that of  $COV_s$ .

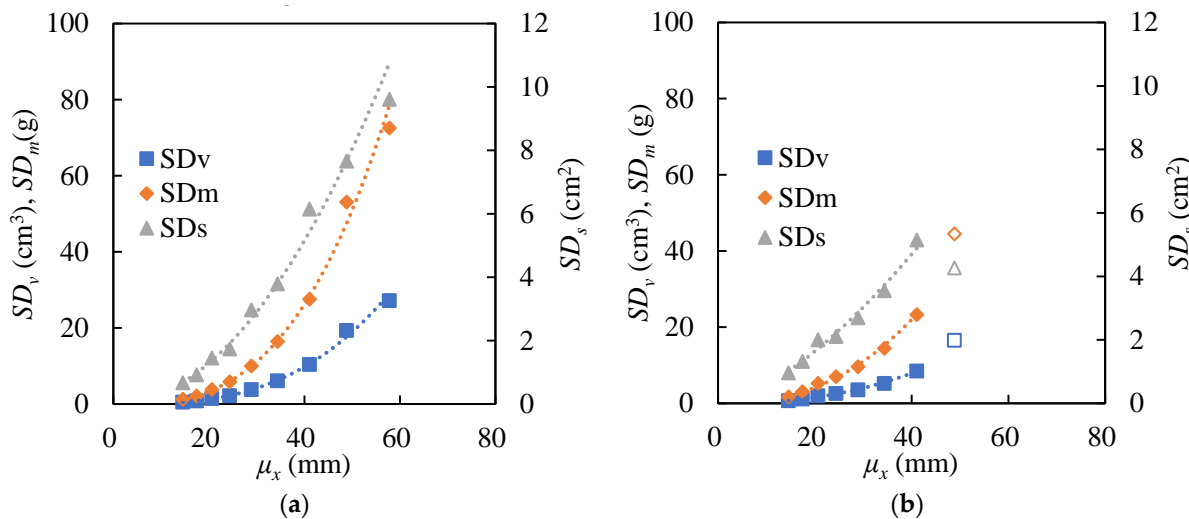


**Figure 9.** Relationship of  $SD_v$ ,  $SD_m$ , and  $SD_s$  values to  $\mu_x$  values of different sizes for Ore A (a) and Ore B (b). (Hollow symbol represents the outlier of the data series with the same shape).

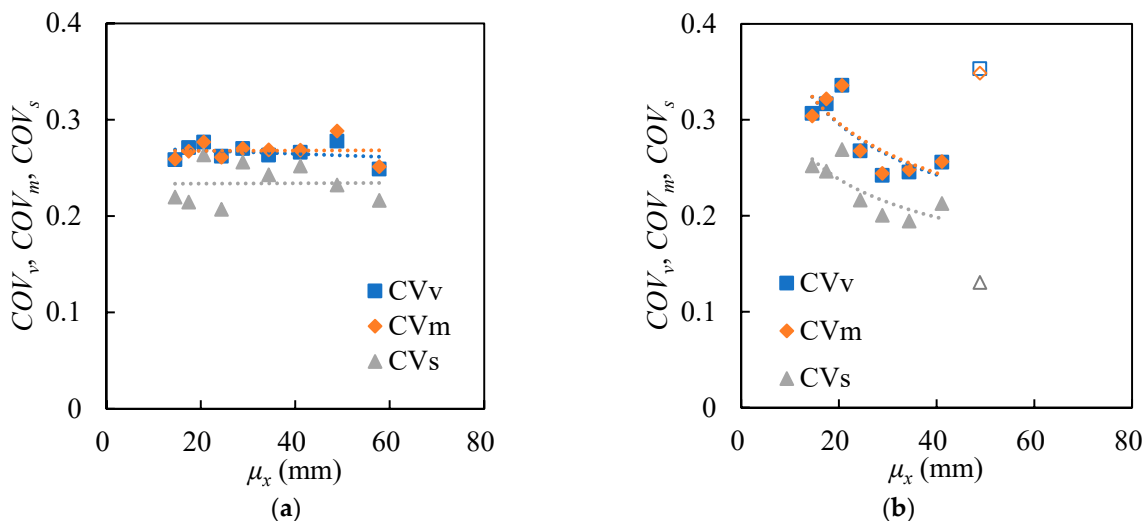


**Figure 10.** Relationship of  $COV_v$ ,  $COV_m$ , and  $COV_s$  values to  $\mu_x$  values of different sizes for Ore A (a) and Ore B (b). (Hollow symbol represents the outlier of the data series with the same shape).

### 3.2.3. Ore Particle Properties of Specific Gravity, Circularity, and Aspect Ratio

The relationships of the  $SD_{sg}$ ,  $SD_c$ ,  $SD_{ar}$ ,  $COV_{sg}$ ,  $COV_c$ , and  $COV_{ar}$  values to the  $\mu_x$  value for Ore A and Ore B are given in Figures 11 and 12. It can be found that in most cases, the variability of specific gravity, circularity, and aspect ratio of individual particles of both ore samples, either evaluated by SD or by COV, decreases with the increase in  $\mu_x$ . As the value of  $\mu_x$  increases, the variability of the SD or COV values of the Ore B sample is apparently more significant than the Ore A sample. The reduction of shape parameters

(circularity and aspect ratio) in variability at the coarser end may also be caused by the limit of discharge gap of the lab jaw crusher used to prepare Ore B. But the change in  $SD_{sg}$  of the Ore B sample with  $\mu_x$  can be attributed to the occurrence of selective breakage mentioned in Section 3.1.3. The trend indicates that disintegration along the boundary between denser and lighter components had happened for the Ore B sample during crushing, leading to an increased  $SD_{sg}$  value at the finer size. For example, the minimum and maximum specific gravity of individual particles ( $X_{sg}$ ) of Ore B sample in 13.2–16 mm are 1.96 and 4.13, respectively, while the  $X_{sg}$  of 45–53 mm particles varies in a narrow range of 2.73 to 2.82. In comparison, the  $SD_{sg}$  and  $COV_{sg}$  values of the Ore A sample keep unchanged on the whole, despite fluctuations. Linear regression analysis by Excel was also applied to the  $SD_{sg} - \mu_x$  relations and the  $COV_{sg} - \mu_x$  relations of Ore A, and the variance analysis indicates that the slope of the linear relation is 0. As given in Table 2, the 95% confidence interval of the  $SD_{sg}$  value of Ore A sample is determined to be  $0.097 \pm 0.013$ .

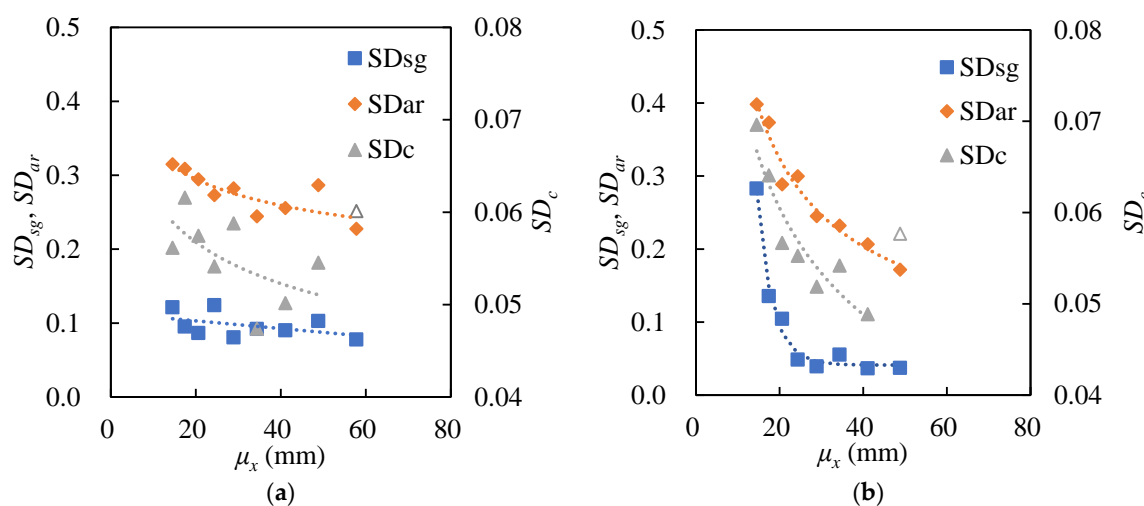


**Figure 11.** Relationships of  $SD_{sg}$ ,  $SD_{ar}$ , and  $SD_c$  values to  $\mu_x$  values of different sizes for Ore A (a) and Ore B (b). (Hollow symbol represents the outlier of the data series with the same shape).

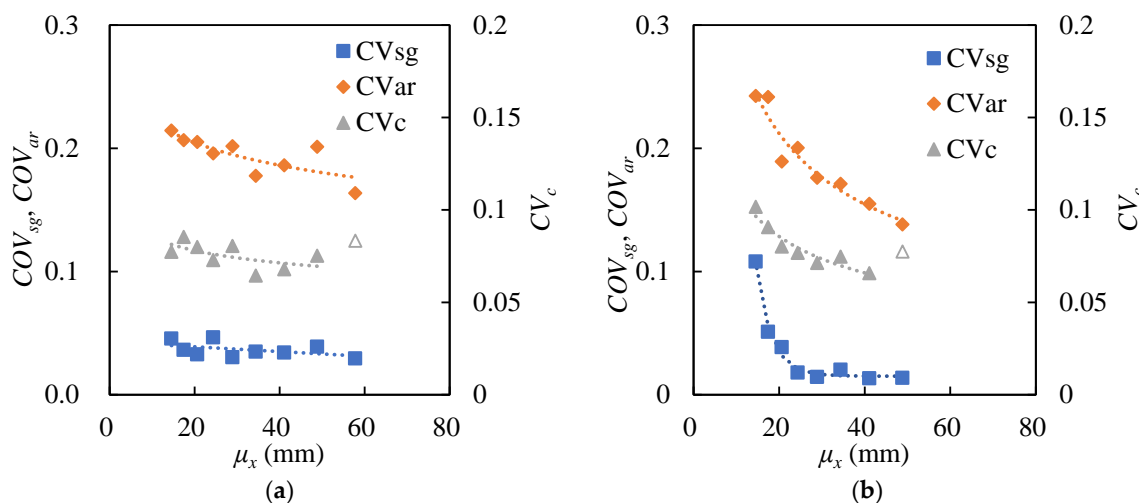


**Figure 12.** Relationship of  $COV_{sg}$ ,  $COV_{ar}$ ,  $COV_c$  values to  $\mu_x$  values of different sizes for Ore A (a) and Ore B (b). (Hollow symbol represents the outlier of the data series with the same shape).

### 3.3. Distribution of Different Ore Particle Properties

The distribution of each property-size data set is identified using the method introduced in Section 2.4. For each particle property of a given ore type, the distribution that generates a  $p$ -value greater than the significance level (0.05) in all or almost all size fractions

is accepted. If more than two distributions meet this criterion, the simplest distribution that fits the data well is preferred. Distributions of the same type but with more parameters are only chosen when the *p*-value of the likelihood-ratio test (LRT) is smaller than 0.05. This test is completed by Minitab software. For instance, for a 3-parameter Weibull distribution, the likelihood-ratio test compares the fit of the 3-parameter Weibull distribution family with the fit of the Weibull distribution family (a subset with the third parameter set as 0). If a 3-parameter Weibull distribution significantly improves the fit, then the *p*-value for the likelihood-ratio test statistic is very small. The significance level of 0.05 is applied in this study.

The best-fitted distributions of different particle properties determined by the goodness-of-fit test for both ore types are listed in Table 3. Here, the distribution of porosity is chosen only for Ore A particles in 22.4–26.5 mm. In contrast, the distributions of other particle properties are chosen for both ore types based on the fitting results of all size fractions.

**Table 3.** Best fitted distribution determined by goodness-of-fit test for Ore A and Ore B.

Property	Distribution	Mean of GFT <i>p</i>		Mean of LRT <i>p</i>	
		Ore A	Ore B	Ore A	Ore B
Length	Largest extreme value	>0.139 *	>0.245 *	/	/
Width	Normal	0.337	0.512	/	/
Height	Weibull: Ore A	>0.202 *	>0.316 *	/	0.048
	3-parameter Weibull: Ore B				
Volume	Lognormal	0.552	0.317	/	/
Mass	Lognormal	0.505	0.325	/	/
Area	Lognormal	0.276	0.387	/	/
Specific gravity	Logistic	>0.195 *	>0.152 *	/	/
Circularity	Weibull	>0.185 *	>0.195 *	/	/
Aspect ratio	3-parameter Weibull	>0.250 *	>0.296 *	0.000	0.000
Porosity	3-parameter Weibull	>0.5 *	/	0.000	/

\* In some cases, the *p*-value of the goodness-of-fit test is given as a range, leading to the existence of a greater-than sign in the table. GFT *p*: *p*-value for a goodness-of-fit test; LRT *p*: *p*-value for likelihood-ratio test.

Histogram of  $X_l$ ,  $X_h$ ,  $X_v$ ,  $X_m$ ,  $X_s$ ,  $X_{sg}$ ,  $X_{ar}$ ,  $X_c$ , and  $X_p$  values of Ore A particles in 22.4–26.5 mm are given in Figure 13 for illustration, together with the fitted distribution curves. As 22.4–26.5 mm is the only size fraction of which the  $X_w$  values of individual Ore A particles fail to provide the normal distribution, the histogram of  $X_w$  values of Ore A in 19–22.4 mm is illustrated instead. For all kinds of distributions listed in Table 3, the PDFs can be determined with 2 or 3 parameters out of the location, scale, shape, and threshold parameters. The values of corresponding parameters for the PDFs are also labeled in Figure 13.

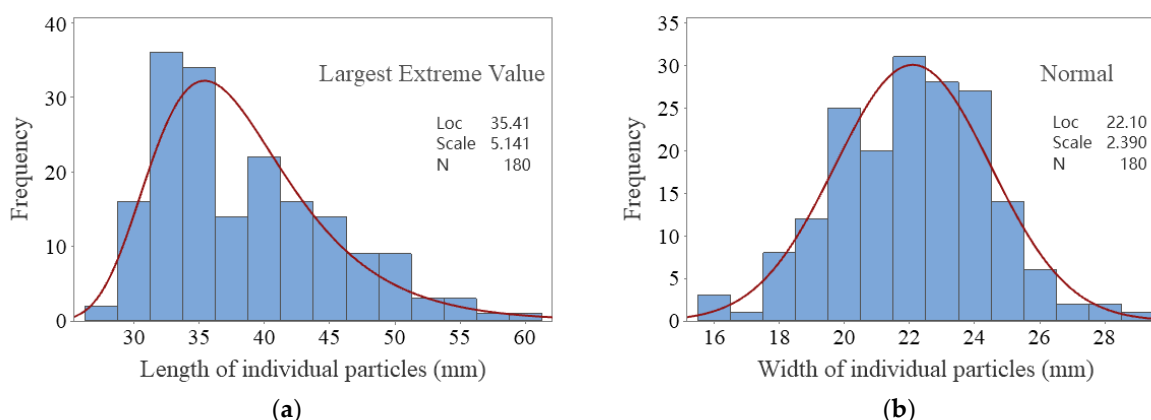


**Figure 13.** Cont.

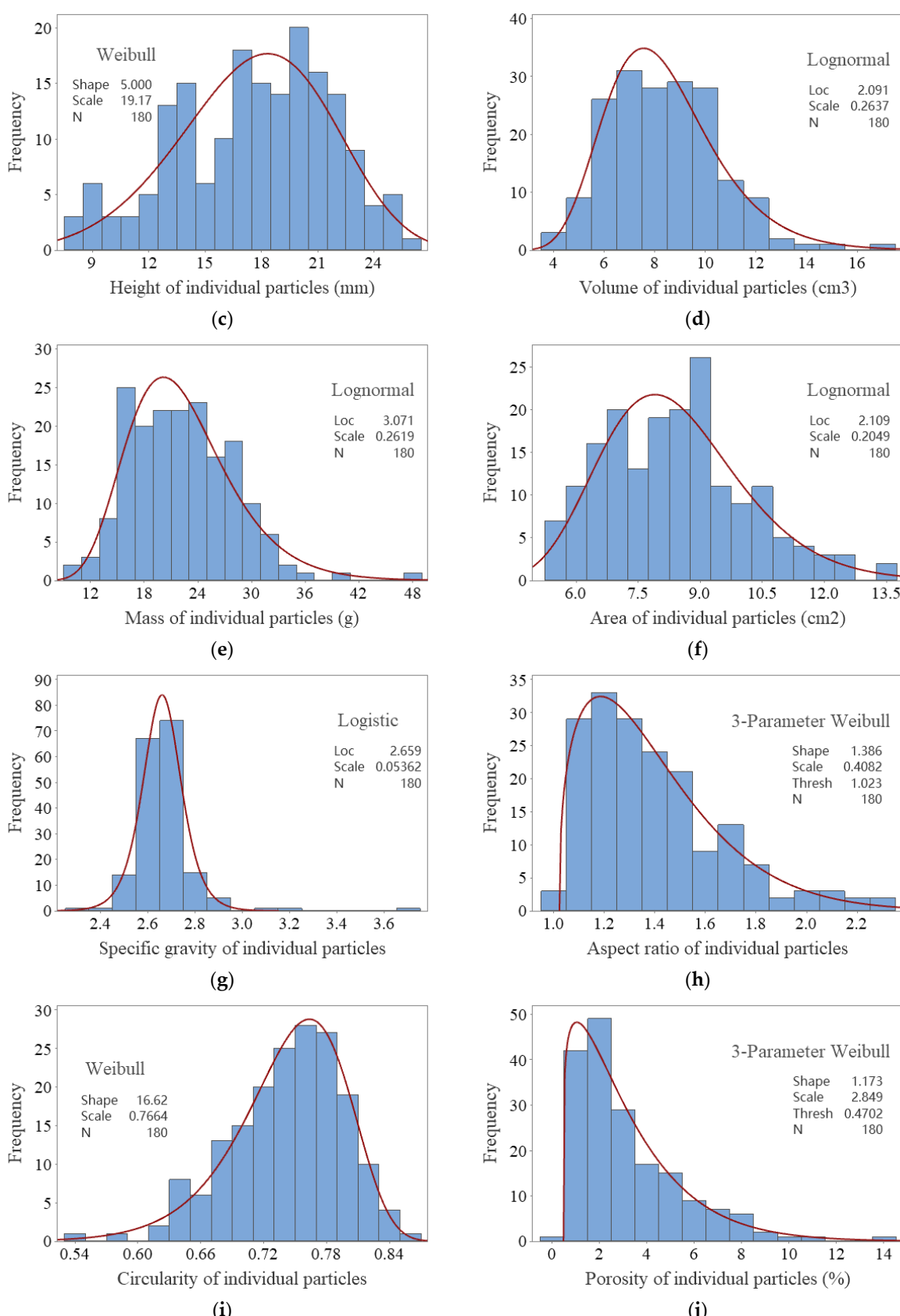


**Figure 13.** Histogram of individual particle's (a) Length, (b) Width, (c) Height, (d) Volume, (e) Mass, (f) Area, (g) Specific gravity, (h) Aspect ratio, (i) Circularity and (j) Porosity of Ore A sample. (Particle width is of 19–22.4 mm while all other properties are of 22.4–26.5 mm).

### 3.3.1. Ore Particle Properties of Length, Width, and Height

The distributions provide the best fit for the  $X_l$ ,  $X_w$ , and  $X_h$  values in different size fractions for Ore A and Ore B and are identified as the largest extreme value distribution, normal distribution, and Weibull distribution, as illustrated in Figure 13a–c. The largest extreme value distribution is defined by its location and scale parameters. Compared with a normal distribution of the same location and scale parameters, the largest extreme value distribution is skewed to the right to describe the large values observed. Unlike the direction along width and height, individual ore particles are allowed to pass through the sieve aperture in a lengthwise direction. Therefore, extremely large values of  $X_l$  are allowed to emerge in a given size fraction. In this study,  $X_w$  is the only property following normal distribution, though normal distribution is the most common statistical distribution in many fields. In comminution, the Weibull distribution was used to model the probability and size reduction degree of breakage [12]. As the height of particles is mainly subject to the discharge gap of the crusher, it is not unexpected that the (3-parameter) Weibull distribution fits the  $X_h$  data sets best. The Weibull distribution is described by the shape and scale parameters. For the 3-parameter Weibull distribution, the threshold parameter is added to describe the shift of the distribution away from 0. This shift possibly reflects the effect of the lab jaw crusher used to prepare the Ore B sample.

### 3.3.2. Ore Particle Properties of Volume, Mass, and Area

The  $X_v$ ,  $X_m$ , and  $X_s$  data sets of Ore A and Ore B can be fitted well with a lognormal distribution, as illustrated in Figure 13d–f. This means the natural logarithm of the  $X_v$ ,  $X_m$ , and  $X_s$  values in a given size fraction follow a normal distribution. The normal distribution generally describes processes whose values result from adding many small variations. While the values result from the multiplication of many small variations, the lognormal distribution is a better descriptor of the process [13]. Since the volume, mass, and area of an individual ore particle are proportional to the product of the particle's length, width, height, and specific gravity, it is as expected that the  $X_v$ ,  $X_m$ , and  $X_s$  data sets follow a lognormal distribution.

### 3.3.3. Ore Particle Properties of Specific Gravity

Initially, no distribution could pass the significance level of the goodness-of-fit test when fitting the  $X_{sg}$  data sets. Observation of the  $X_{sg}$  data sets suggests some discrete, tremendous values exist. For example, the largest three values of specific gravity for Ore A particles in 22.4–26.5 mm are 3.65, 3.21, and 3.12, respectively, while 175 out of the rest 177 particles are of specific gravity in a narrow range of  $2.66 \pm 0.23$  (Figure 13g). Therefore, all particles with a specific gravity higher than three were removed before conducting a goodness-of-fit test. The number of such particles with an extremely large specific gravity in each size fraction is minimal, being approximately 1.4 and 2.5 on average for the different size fractions of Ore A and Ore B samples, respectively. The extremely large specific gravity of such particles can be attributed to the concentration of sulfide minerals in an individual particle. Finally, logistic distribution is identified as appropriate for  $X_{sg}$  data sets for Ore A and Ore B.

The shape of the logistic distribution is similar to that of the normal distribution. However, the logistic distribution has longer tails and higher kurtosis than a normal distribution. For Ore A and Ore B, the  $X_{sg}$  values in a given size fraction are distributed relatively narrowly. Therefore, logistic distribution is more suitable than normal distribution to describe the distribution of particle-specific gravity.

### 3.3.4. Ore Particle Properties of Circularity, Aspect Ratio, and Porosity

Similar to the  $X_h$  data sets, the data sets of  $X_c$ ,  $X_{ar}$ , and  $X_p$  of Ore A and Ore B can also be fitted well with the Weibull or 3-parameter Weibull distribution, as illustrated in Figure 13h–j. The Weibull distribution is a versatile distribution that can be used to model a wide range of applications in engineering. One advantage of the Weibull distribution is that it can fit distributions with different distribution curve shapes well. A Weibull

distribution with a shape parameter equal to three has a curve that approximates to normal distribution. A low value for shape, say 1, gives a right-skewed curve, while a high value, states 10, provides a left-skewed curve. As illustrated in Figure 13,  $X_h$  and  $X_c$  data sets with shape parameters being 5.00 and 16.62 exhibit left-skewed distribution curves. The shape parameters of the  $X_{ar}$  and  $X_p$  data sets are 1.37 and 1.17, respectively. Accordingly, the curves of these two data sets are right-skewed.

More details about the parameters of distribution functions are discussed in Section 3.4, as well as the attempt to predict these parameters by particle size.

### 3.4. Prediction of the Distribution of Particle Properties in a Given Size Fraction

As mentioned above, the PDFs of all the distributions listed in Table 3 can be determined by 2 or 3 parameters out of 4 parameters, i.e., location ( $\alpha$ ), scale ( $\beta$ ), shape ( $\gamma$ ), and threshold ( $\delta$ ). According to statistical theory, the mathematic expectation ( $\mu$ ) and variance ( $\sigma^2$ ) of the distributions listed in Table 3 are dependent variables of  $\alpha$ ,  $\beta$ ,  $\gamma$ , and  $\delta$ . Considering the  $\mu$  and  $\sigma$  values of individual particle properties (except porosity) in a given size fraction can be predicted by particle size with the models listed in Tables 1 and 2, it is feasible to predict the distribution of the property-size data sets of Ore A and Ore B samples by the  $\mu_x$  value.

#### 3.4.1. Prediction of Function Parameters for Different Distributions

While detailed derivation are given in Appendix A, the relations of  $\alpha$ ,  $\beta$ ,  $\gamma$ , and  $\delta$  to  $\mu$  and  $\sigma$  are summarized below:

##### 1. Normal and logistics distributions

Normal and logistics distributions are the best-fitted distributions for  $X_w$  and  $X_{sg}$  data sets of Ore A and Ore B. The common feature of these two kinds of distributions is that the mathematic expectation depends solely on the  $\alpha$  parameter while the variance is only decided by the  $\beta$  parameter.

The  $\mu$  and  $\sigma$  values of each property-size data set can be determined by the models listed in Tables 1 and 2. Therefore, the parameters of the PDFs of  $X_w$  and  $X_{sg}$  data sets of Ore A and Ore B can be predicted with Equations (1) and (2).

For normal distribution, there is:

$$\begin{cases} \alpha = \mu \\ \beta = \sigma \end{cases} \quad (1)$$

For logistics distribution, there is:

$$\begin{cases} \alpha = \mu \\ \beta = \frac{\sqrt{3}}{\pi} \sigma \end{cases} \quad (2)$$

##### 2. Largest extreme value and lognormal distributions

The  $X_v$ ,  $X_m$ ,  $X_s$ , and  $X_l$  data sets of the Ore A and Ore B samples can be described by lognormal and largest extreme value distributions, respectively. For the largest extreme value distribution, the variance depends solely on the  $\beta$  parameter; In contrast, both distributions' mathematic expectations and the lognormal distribution's variance are determined by  $\alpha$  and  $\beta$  parameters together.

The  $\mu$  and  $\sigma$  values of each property-size dataset can be determined by the models listed in Tables 1 and 2. Therefore, the parameters of the PDFs of  $X_v$ ,  $X_m$ ,  $X_s$ , and  $X_l$  data sets of Ore A and Ore B can be predicted with Equations (3) and (4).

For largest extreme value distribution, there is:

$$\begin{cases} \alpha = \mu - E \frac{\sqrt{6}}{\pi} \sigma \\ \beta = \frac{\sqrt{6}}{\pi} \sigma \end{cases} \quad (3)$$

For lognormal distribution, there is:

$$\begin{cases} \alpha = \ln\mu - 0.5 \left( \ln\left(\frac{\sigma^2}{\exp(2\ln\mu)} + 1\right) \right) \\ \beta = \sqrt{\ln\left(\frac{\sigma^2}{\exp(2\ln\mu)} + 1\right)} \end{cases} \quad (4)$$

### 3. Weibull and 3-parameter Weibull distribution

The  $X_h$ ,  $X_c$ , and  $X_{ar}$  data sets of the Ore A and Ore B samples can be described by Weibull or 3-parameter Weibull distribution. The form of these two distributions is dependent on  $\beta$ ,  $\gamma$ , and  $\delta$ . There is no analytic functions for these parameters, such as other distributions discussed above. However, on the premise that the value of  $\delta$  is known, the value of  $\beta$  and  $\gamma$  can be determined from  $\sigma$  and  $\mu$ . For Weibull distribution, which is followed by  $X_c$  data sets for both ore types and  $X_h$  data sets for Ore A, the value of  $\delta$  is set as zero. The  $X_{ar}$  data sets of both ore types follow 3-parameter Weibull distribution. However, it was found that the  $\delta$  values of the aspect ratio of both ore types are approximately 1. This is consistent with the definition of aspect ratio. At the present stage, the  $\delta$  value for the  $X_h$  data set of the Ore B sample cannot be predicted by  $\sigma$  and  $\mu$ . The threshold of the  $X_h$  value of Ore B is possibly caused by applying a lab jaw crusher with a small discharge gap rather than by an industrial secondary crusher. Alternatively, the relation of  $\delta$  to  $\mu_x$  for  $X_h$  data sets of the Ore B sample from experiment (Figure 14) is adopted.

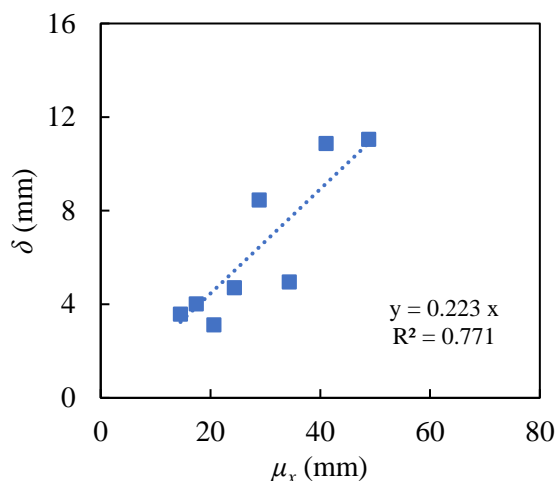


**Figure 14.** Relation of  $\delta$  to  $\mu_x$  for  $X_h$  data sets of Ore B sample.

The procedure to determine  $\beta$  and  $\gamma$  values numerically from  $\delta$  is described detailedly in Appendix A.3.

#### 3.4.2. Model Validation

The method to predict the distribution functions of individual particles' properties in a given size fraction is validated with the property-size data sets of Ore A and Ore B, except  $X_p$  (porosity). The model fitting results for the two kinds of ore samples are shown in the Figures A2 and A3 of Appendix A respectively.

The results suggest that the method noted above can predict the location ( $\alpha$ ), scale ( $\beta$ ), shape ( $\gamma$ ) parameters, and threshold ( $\delta$ ) well, with an  $R^2$  value very close to 1. Note that for the Ore A sample, the  $\delta$  parameter applies only to the  $X_{ar}$  data sets and is fixed at 1 in the prediction. Hence the  $R^2$  value for fitting the  $\delta$  parameter is not available (Figure A2d). Since the  $\delta$  parameter is fixed at 1 for  $X_{ar}$  data sets, the  $R^2$  value for the fitting of the  $\delta$  parameter is calculated only for the  $X_h$  data sets of Ore B (Figure A3d). Here, the threshold ( $\delta$ ) parameter is predicted by the  $\delta$ - $\mu_x$  relation shown in Figure 12. The fitting quality for the threshold ( $\delta$ ) parameter is lower than other parameters ( $R^2 = 0.771$ ), but it is still acceptable in this application scenario.

In conclusion, the data sets of individual ore particles of the same property (geometry, mass, and density) in different size fractions tend to follow the same kind of distribution. Parameters of the distribution functions of a given property-size data set can be predicted from the geometric mean size of its size fraction using the models developed in this study. With the porosity data limited to one size fraction, the 3-parameter Weibull distribution was identified as the best-fit distribution of the individual particles' porosity for Ore A. However, further work is needed to detailedly explore the statistical characteristics of the porosity of individual ore particles for different ore types and size fractions.

### 3.5. Potential Applications and Further Works

The ability to precisely describe and predict the statistical characteristics of individual ore particles' properties provides a new technical tool for intelligent mineral processing. By way of example, the following three concepts of application of this technical tool are discussed. Note that this does not exclude other potential applications.

#### 3.5.1. Precisely Processing according to the Statistical Characteristics of Individual Particles

This study provides a preliminary trial to describe and predict the statistical characteristics of individual ore particles' properties. However, the kinds of particle properties are limited in geometry, density, and porosity. The statistical description of processing objects in mineral concentration can be integrated with the concept of geometallurgy. Geometallurgy refers to the dynamic integration of geological data with small-scale physical measurements to define the spatial variability of a deposit and aid the prediction of metallurgical performance [14]. In each spatial location, metallurgical testing is conducted to measure the averaged properties of ore particles. With the method developed in this study, the distribution of individual ore particles' properties for each spatial location can be described and predicted. The statistical characteristics for feed to mineral concentrator are helpful to design processing flowsheet and monitoring and controlling the processing circuits precisely. However, there are two gaps in the realization of this vision.

Firstly, the properties of individual ore particles investigated in this study are limited to three types, i.e., geometry, density, and porosity. The statistical characteristics of other metallurgical properties, say metal grade, grain size, mineral types, etc., are necessary to be investigated in future works. Attention must also be paid to the statistical characteristics of individual ore particles' properties in a size range below 13.2 mm.

Secondly, measuring the properties of individual ore particles is tedious and time-consuming, so it is unaffordable to carry out such investigation as a matter of routine. Online automatic measuring of individual ore particles' geometry is not difficult to realize. However, innovative technologies are required to automatically, quickly, and cheaply obtain the statistical characteristics of individual ore particles' properties of, say, metal grade, grain size, mineral types, etc. Furthermore, efforts are needed to develop a methodology to predict the spatial variation of the statistical characteristics of individual ore particles' properties to reduce the data collection workload.

#### 3.5.2. Preparation of Feed Sample for Lab-Scale Testing

It is a common practice for lab-scale testing to prepare feed samples with a lab jaw crusher. For example, a feed sample directly collected from the mine site is preferred for JK Drop Weight Test (JKDWT), which is a testing work that aims to measure ore competence index  $A \times b$  value. The standard JKDWT uses particles sample in five size fractions ranging between 13.2 mm and 63 mm [15]. Due to the ore availability limitation, sometimes run-of-mine ore particles coarser than 63 mm were broken by a lab jaw crusher to generate feed samples of the top-size fractions. The influence of using lab jaw crusher products as a feed sample was not evident in the past. However, the effect of the crushing method on the dimensions of the Ore B sample, as mentioned in Section 3.1, suggests that the product of the lab jaw crusher may have distinct geometry characteristics compared to the sample collected from the industrial crusher product. A study was conducted to compare the

breakage behavior in JKDWT between flaky and equidimensional shapes, and the result indicated that the shape of a particle influences the product size distribution of JKDWT [3]. According to the discovery in this study, remedies to this problem would be calibrating the testing result to offset the influence of sample variation or selecting progeny particles from the lab jaw crusher product to constitute a feed sample of which the distribution of individual particles' geometry, mass and density parameters is similar to that of industrial crusher product. The PDFs of the unavailable "industrial" particles in top-size fractions can be predicted from the "industrial" particles in finer size fractions using the method developed in this study.

The method developed in this study can also be applied to improve the feed sample preparation for other lab-scale tests which are susceptible to the size and shape of feed particles, such as bulk density, angle of repose, gravity separation, column leaching, etc. It is suggested that if a lab jaw crusher has to be used to prepare feed samples for these tests, the feed sample should be prepared by selecting particles having a distribution of properties similar to industrial crusher products.

### 3.5.3. Calibration of Ore Particle Size Image Analysis

Image analysis of ore particle size distribution has been widely applied in the online detection system of mineral concentrators. However, ore particle size distribution obtained by image analysis is not unique for the same product. The obtained results are dependent on both the size and shape of ore particles [16] as well as the representability of ore particles. Determining the PDFs of individual ore particles' geometry can provide calibration for the image analysis of ore particle size distribution in two ways. Firstly, the statistical characteristics of individual particles' shapes can be integrated into the algorithm to convert particle shapes into particle sizes. This may require further statistical investigation into more kinds of shape parameters that are related to particle size. Secondly, the statistical characteristics of individual particles' shape detected by image analysis can be compared with that predicted by the method developed in this study to "adjust" the size distribution obtained.

### 3.5.4. Influence of Mineralogy and Crushing Process on Particle Morphological Properties

Mineralogy and crushing process had been identified as the main aspects that influence the rock shape properties [17–19]. However, the effect of mineralogy and morphological properties on ore breakage behavior have not yet been fully understood. Although the work presented in this paper mainly focus on the statistical description of ore particles' properties, it is crucial to investigate how mineralogy and crushing process interact with each other to influence the shape of ore particles so as to learn how to manage it for best economic results. The statistical method to describe the morphological properties of particles was developed with two kinds of porphyry copper ores only. In the future work, more samples of different ore types are required for further validation of the method, and investigation of the relation between mineralogy, crushing process and particle morphological properties is required.

## 4. Conclusions

A statistical study on the geometry, mass, specific gravity, and porosity of individual ore particles is conducted for two kinds of porphyry copper ores. The statistical characteristics of each property-size data set are investigated in terms of central tendency, variability, and probability density function.

It was found that the mean value and the standard deviation of the same particle property can either be predicted from particle size or be approximated by a constant. The best-fit distribution of each kind of particle property was identified by the Anderson-Darling test using Minitab software. Generally, the data sets with the same particle property but different size fractions and ore types follow the same distribution. With the method developed in this study, the PDF for each property-size data set can be predicted from

the corresponding  $\mu^x$  value. Generally, the method can fit the parameters of distribution functions well.

The ability to describe and predict the distribution of individual ore particles' properties can improve the precise processing of ore feed in concentrators, the preparation of feed samples for lab-scale testing, the calibration of image analysis of ore particle size distribution, etc. Further work is required in the future to improve the methodology.

**Author Contributions:** Conceptualization, methodology, writing—original draft preparation, supervision, W.Z.; methodology, investigation, writing—original draft preparation, Y.L.; supervision, validation, visualization, J.X.; methodology, investigation, W.L.; writing—review and editing, K.C. All authors have read and agreed to the published version of the manuscript.

**Funding:** This research was funded by the National Natural Science Foundation of China (grant number 52074091), Fujian Province Natural Science Fund (grant number 2020J01511), and Jinan Heavy Machinery Joint-stock Co., Ltd.

**Data Availability Statement:** Not applicable.

**Acknowledgments:** We sincerely thank the editor and reviewers for their constructive comments which helped in improving our paper.

**Conflicts of Interest:** The authors declare no conflict of interest.

## Appendix A

### Appendix A.1. Prediction of Function Parameters for Normal and Logistics Distributions

The PDF of the normal distribution is given in Equation (A1).

$$f(x) = \frac{1}{\sqrt{2\pi}\beta} \exp\left(\frac{-(x-\alpha)^2}{2\beta^2}\right), \beta > 0 \quad (\text{A1})$$

For the normal distribution, there is:

$$\begin{cases} \alpha = \mu \\ \beta = \sigma \end{cases} \quad (\text{A2})$$

As for the logistic distribution, PDF can be expressed as in Equation (A3).

$$f(x) = \frac{\exp\left(-\frac{x-\alpha}{\beta}\right)}{\beta \left[1 + \exp\left(-\frac{x-\alpha}{\beta}\right)\right]^2}, -\infty < x < \infty, -\infty < \alpha < \infty, \beta > 0 \quad (\text{A3})$$

For the logistics distribution, there is:

$$\begin{cases} \mu = \alpha \\ \sigma^2 = \frac{\beta^2\pi^2}{3} \end{cases} \quad (\text{A4})$$

This can be converted into:

$$\begin{cases} \alpha = \mu \\ \beta = \frac{\sqrt{3}}{\pi}\sigma \end{cases} \quad (\text{A5})$$

### Appendix A.2. Prediction of Particle Properties with the Largest Extreme Value and Lognormal Distributions

PDF of the largest extreme value distribution is given in Equation (A6).

$$f(x) = \left(\frac{1}{\beta}\right) \exp\left[\frac{(\alpha-x)}{\beta}\right] \exp\left\{-\exp\left[\frac{(\alpha-x)}{\beta}\right]\right\} \quad (\text{A6})$$

For the largest extreme value distribution, there is:

$$\begin{cases} \mu = \alpha + E\beta \\ \sigma^2 = \pi^2\beta^2/6 \end{cases} \quad (\text{A7})$$

Here,  $E$  is the Euler constant and  $\approx 0.57722$ .

Substituting the relationship of  $\beta$  to  $\sigma$  into the first subequation, Equation (A7) can be converted into:

$$\begin{cases} \alpha = \mu - E\frac{\sqrt{6}}{\pi}\sigma \\ \beta = \frac{\sqrt{6}}{\pi}\sigma \end{cases} \quad (\text{A8})$$

The PDF of the lognormal distribution is given in Equation (A9).

$$f(x) = \frac{1}{\beta x \sqrt{2\pi}} \exp\left(-\frac{(\ln(x) - \alpha)^2}{2\beta^2}\right), x > 0, \beta > 0 \quad (\text{A9})$$

For the lognormal distribution, there is:

$$\begin{cases} \mu = \exp(\alpha + 0.5\beta^2) \\ \sigma^2 = \exp(2\alpha + \beta^2)(\exp(\beta^2) - 1) \end{cases} \quad (\text{A10})$$

Rewrite Equations (A10)–(A12) as the following:

$$\alpha = \ln\mu - 0.5\beta^2 \quad (\text{A11})$$

$$\beta = \sqrt{\ln\left(\frac{\sigma^2}{\exp(2\ln\mu)} + 1\right)} \quad (\text{A12})$$

By substituting Equation (A12) into Equation (A11),  $\alpha$  can be expressed as:

$$\alpha = \ln\mu - 0.5\left(\ln\left(\frac{\sigma^2}{\exp(2\ln\mu)} + 1\right)\right) \quad (\text{A13})$$

#### Appendix A.3. Prediction of Particle Property with (3-parameter) Weibull Distribution

The PDF of the 3-parameter Weibull distribution is given in Equation (A14).

$$f(x) = \frac{\gamma}{\beta^\gamma} (x - \delta)^{\gamma-1} \exp\left[-\left(\frac{x - \delta}{\beta}\right)^\gamma\right], x \geq \delta, \beta \geq 0, \gamma \geq 0 \quad (\text{A14})$$

The mathematic expectation and variance of 3-parameter Weibull can be expressed as:

$$\begin{cases} \mu = \beta\Gamma\left(1 + \frac{1}{\gamma}\right) + \delta \\ \sigma^2 = \beta^2\left(\Gamma\left(1 + \frac{2}{\gamma}\right) - \Gamma^2\left(1 + \frac{1}{\gamma}\right)\right) \end{cases} \quad (\text{A15})$$

Here,  $\Gamma$  represents the gamma function. When  $x$  is a real number larger than 0, the gamma function can be expressed as:

$$\Gamma(x) = \int_0^{+\infty} t^{x-1} e^{-t} dt \quad (\text{A16})$$

From Equation (A15), the relationship below can be derived:

$$\beta = \frac{\mu - \delta}{\Gamma\left(1 + \frac{1}{\gamma}\right)} \quad (\text{A17})$$

Substitute Equation (A17) into the second subequation in Equation (A15) and make the necessary conversion, that is:

$$\frac{\Gamma\left(1 + \frac{2}{\gamma}\right)}{\Gamma^2\left(1 + \frac{1}{\gamma}\right)} = \frac{\sigma^2}{(\mu - \delta)^2} + 1 \quad (\text{A18})$$

Hereinafter,  $\Gamma\left(1 + \frac{1}{\gamma}\right)$ ,  $\frac{\Gamma\left(1 + \frac{2}{\gamma}\right)}{\Gamma^2\left(1 + \frac{1}{\gamma}\right)}$ , are represented as  $G_1$  and  $G_2$ , respectively. It is impossible to derive an analytic function for  $\gamma$  from Equation (A18). However,  $G_1$  and  $G_2$  are monotonic continuous functions when  $\gamma > 0$ , as illustrated in Figure A1. This means that a given value on the right side of Equation (A18) corresponds to a unique value of  $\gamma$ . On the premise that the value of  $\delta$  is known, the value of  $\gamma$  can be determined from the  $\sigma$  and  $\mu$  of a given data set according to Equation (A18).

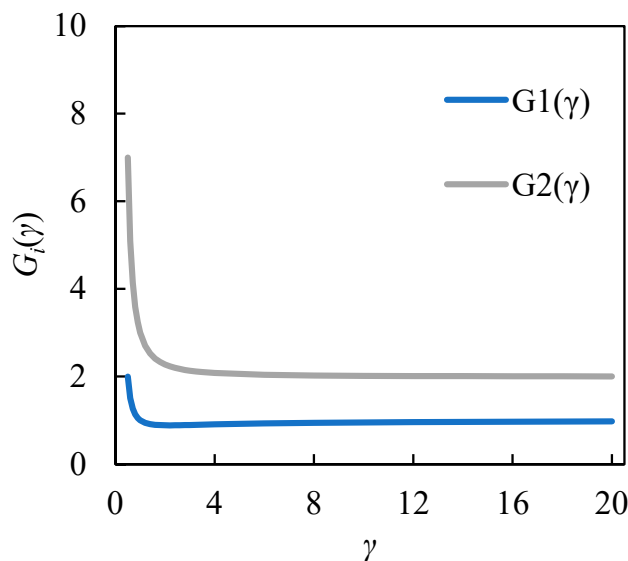


**Figure A1.** Function curves for  $G_1$  and  $G_2$ .

From Equation (A17), it can be derived that:

$$\begin{cases} \beta = \frac{\mu - \delta}{\Gamma\left(1 + \frac{1}{\gamma}\right)} \\ \beta = \sqrt{\frac{\sigma^2}{\Gamma\left(1 + \frac{2}{\gamma}\right) - \Gamma^2\left(1 + \frac{1}{\gamma}\right)}} \end{cases} \quad (\text{A19})$$

Once the values of  $\gamma$  and  $\delta$  are known, the value of  $\beta$  can be calculated from either subequation of Equation (A18). The key to obtaining  $\beta$  and  $\gamma$  is to determine the value of  $\delta$ , which was discussed in Section 3.4.1.

#### Appendix A.4. Figures of Fitting the Parameters of PDFs for Ore Particle Properties

Figures A2 and A3 show the model fitting results for the distribution function parameters of particle properties for Ore A and Ore B.

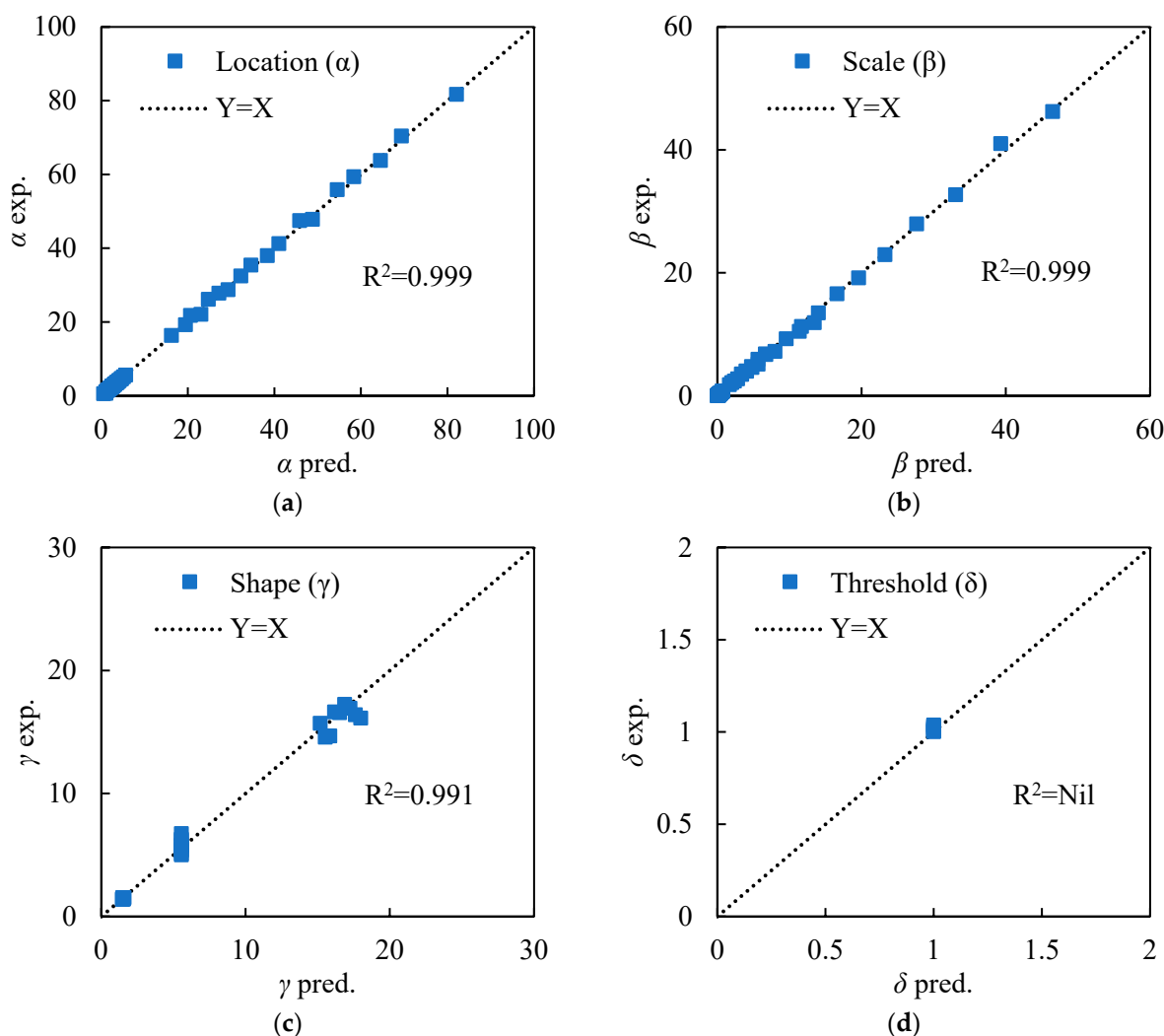


**Figure A2.**  $R^2$  values of fitting the (a)  $\alpha$ , (b)  $\beta$ , (c)  $\gamma$  and (d)  $\delta$  parameters of PDFs for Ore A property-size data sets.

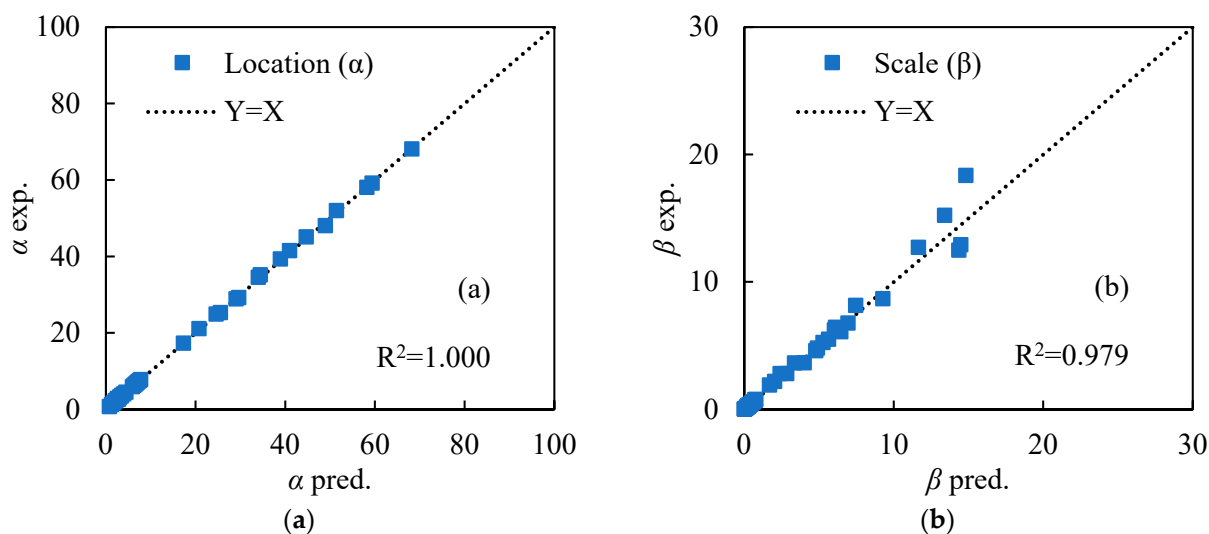


**Figure A3. Cont.**

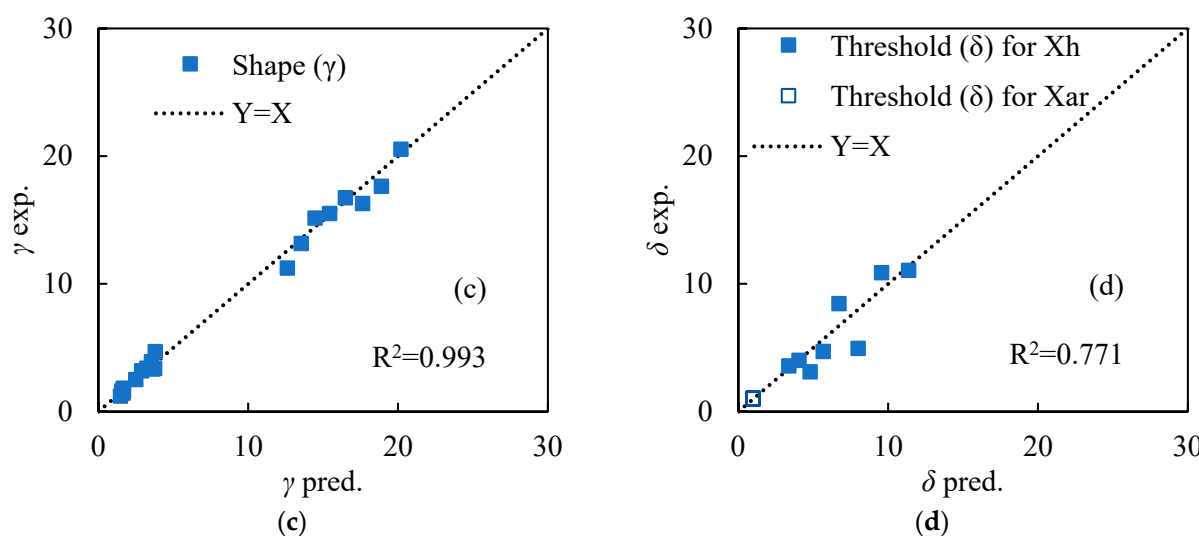


**Figure A3.**  $R^2$  values of fitting the (a)  $\alpha$ , (b)  $\beta$ , (c)  $\gamma$  and (d)  $\delta$  parameters of PDFs for Ore B property-size data sets.

## References

1. Faramarzi, F.; Jokovic, V.; Morrison, R.; Kanchibotla, S.S. Quantifying variability of ore breakage by impact—Implications for SAG mill performance. *Miner. Eng.* **2018**, *127*, 81–89. [[CrossRef](#)]
2. Faramarzi, F.; Napier-Munn, T.; Morrison, R.; Kanchibotla, S.S. The extended drop weight testing approach—What it reveals. *Miner. Eng.* **2020**, *157*, 106550. [[CrossRef](#)]
3. Ulusoy, U. A Review of Particle Shape Effects on Material Properties for Various Engineering Applications: From Macro to Nanoscale. *Minerals* **2023**, *13*, 91.
4. Norazirah, A.; Fuad, S.H.S.; Hazizan, M.H.M. The Effect of Size and Shape on Breakage Characteristic of Mineral. *Procedia Chem.* **2016**, *19*, 702–708. [[CrossRef](#)]
5. Yekeler, M.; Çiftçi, M.; Ulusoy, U.; Özkan, A. Correlation of the Particle Size Distribution Parameters with Sieving Rate Constant. *Part. Sci. Technol. Int. J.* **2014**, *32*, 118–122. [[CrossRef](#)]
6. Wills, B.A.; Finch, J.A. *Wills' Mineral Processing Technology: An Introduction to the Practical Aspects of Ore Treatment and Mineral Recovery*; Butterworth-Heinemann: Oxford, UK, 2016.
7. Burat, E.; Dinç, N.İ.; Dursun, H.N.; Ulusoy, U. The Role of Particle Size and Shape on the Recovery of Copper from Different Electrical and Electronic Equipment Waste. *Minerals* **2023**, *13*, 847. [[CrossRef](#)]
8. Verrelli, D.I.; Bruckard, W.J.; Koh, P.; Schwarz, M.P.; Follink, B. Particle shape effects in flotation. Part 1: Microscale experimental observations. *Miner. Eng.* **2014**, *58*, 80–89. [[CrossRef](#)]
9. Cleary, P.W.F.; Owen, P. Effect of particle shape on structure of the charge and nature of energy utilisation in a SAG mill. *Miner. Eng.* **2019**, *132*, 48–68. [[CrossRef](#)]
10. Minitab Minitab 21 Support. Available online: <https://support.minitab.com/en-us/minitab/21/> (accessed on 22 September 2023).
11. Zuo, W.; Shi, F.; Wielen, K.P.v.d.; Weh, A. Ore particle breakage behaviour in a pilot scale high voltage pulse machine. *Miner. Eng.* **2015**, *84*, 64–73. [[CrossRef](#)]
12. Shi, F.; Kojovic, T. Validation of a model for impact breakage incorporating particle size effect. *Int. J. Miner. Process.* **2007**, *82*, 156–163. [[CrossRef](#)]
13. Napier-munn, T.J. *Statistical Methods for Mineral Engineers-How to Design Experiments and Analyse Data*; Julius Kruttschnitt Mineral Research Centre: Indooroopilly, Australia, 2014.
14. Powell, M.S.; Morrison, R.D. The future of comminution modelling. *Int. J. Miner. Process.* **2007**, *84*, 228–239.
15. Shi, F. A review of the applications of the JK size-dependent breakage model: Part 1: Ore and coal breakage characterisation. *Int. J. Miner. Process.* **2016**, *155*, 118–129. [[CrossRef](#)]
16. Califice, A.; Michel, F.; Dislaire, G.; Pirard, E. Influence of particle shape on size distribution measurements by 3D and 2D image analyses and laser diffraction. *Powder Technol.* **2013**, *237*, 67–75. [[CrossRef](#)]
17. Diógenes, L.; Maia, R.; Bessa, I.; Branco, V.C.; Neto, J.N.; Silva, F. The influence of crushing processes and mineralogy of aggregates on their shape properties and susceptibility to degradation. *Constr. Build. Mater.* **2021**, *284*, 122745.

18. Briggs, C.; Evertsson, C.M. Shape potential of rock. *Miner. Eng.* **1998**, *11*, 125–132. [[CrossRef](#)]
19. Rajan, B.; Singh, D. Comparison of Shape Parameters and Laboratory Performance of Coarse Aggregates Produced from Different Types of Crushing Operations. *J. Mater. Civ. Eng.* **2017**, *29*, 04017044. [[CrossRef](#)]

**Disclaimer/Publisher's Note:** The statements, opinions and data contained in all publications are solely those of the individual author(s) and contributor(s) and not of MDPI and/or the editor(s). MDPI and/or the editor(s) disclaim responsibility for any injury to people or property resulting from any ideas, methods, instructions or products referred to in the content.